THE AXIAL-FIELD SPECTROMETER AT THE CERN ISR

Brookhaven-CERN-Copenhagen-Lund-Rutherford-Tel Aviv Collaboration

H. Gordon, R. Hogue, T. Killian, T. Ludlam, M. Winik and C. Woody

Brookhaven National Laboratory, Upton, New York, USA

D. Burckhart, V. Burkert, O. Botner, D. Cockerill, W.M. Evans,
C.W. Fabjan, T. Ferbel, P. Frandsen, A. Hallgren, B. Heck, M. Harris,
J.H. Hilke, H. Hofmann, P. Jeffreys, G. Kantardjian, G. Kesseler,
J. Lindsay, H.J. Lubatti, W. Molzon, B.S. Nielsen, P. Quéru,
L. Rosselet, E. Rosso, A. Rudge, R.H. Schindler, T. Taylor,
J. v.d. Lans, D.W. Wang, Ch. Wang, W.J. Willis and W. Witzeling

CERN, Geneva, Switzerland

H. Bøggild, E. Dahl-Jensen, I. Dahl-Jensen, Ph. Dam, G. Damgaard,
K.H. Hansen, J. Hooper, R. Møller, S.Ø. Nielsen,
L.H. Olsen and B. Schistad

Niels Bohr Institute, Copenhagen, Denmark

T. Akesson, S. Almehed, G. von Dardel, G. Jarlskog, B. Lörstad,
A. Melin, U. Mjörnmark and A. Nilsson

University of Lund, Sweden

M.G. Albrow, N.A. McCubbin, M.D. Gibson and J. Hiddleston

Rutherford Laboratory, Chilton, Didcot, United Kingdom

O. Benary, S. Dagan, D. Lissauer and Y. Oren

University of Tel Aviv, Israel

Presented by C.W. Fabjan

MASTER

THE AXIAL FIELD SPECTROMETER AT THE CERN ISR
†

Brookhaven-CERN-Copenhagen-Lund-Rutherford-Tel Aviv Collaboration

H. Gordon, R. Hogue, T. Killian, T. Ludlam, M. Winik, C. Woody (BNL);
D. Burckhart, V. Burkert, O. Botner, D. Cockerill, W.M. Evans, C.W. Fabjan,
T. Ferbel, P. Frandsen, A. Hallgren, B. Heck, M. Harris, J.H. Hilke,
H. Hofmann, P. Jeffreys, G. Kantardjian, G. Kesseler, J. Lindsay,
H.J. Lubatti, W. Molzon, B.S. Nielsen, P. Quéru, L. Rosselet, E. Rosso,
A. Rudge, R.H. Schindler, T. Taylor, J. v.d. Lans, D.W. Wang, Ch. Wang,
W.J. Willis, W. Witzeling (CERN); H. Bøggild, E. Dahl-Jensen, I. Dahl-Jensen,
Ph. Dam, G. Damgaard, K.H. Hansen, J. Hooper, R. Møller, S.Ø. Nielsen,
L.H. Olsen, B. Schistad (Copenhagen); T. Akesson, S. Almehed, G. von Dardel,
G. Jarlskog, B. Lörstad, A. Melin, U. Mjörnmark, A. Nilsson (Lund);
M.G. Albrow, N.A. McCubbin, M.D. Gibson, J. Hiddleston (Rutherford);
O. Benary, S. Dagan, D. Lissauer, Y. Oren (Tel Aviv)

(Presented by C.W. Fabjan)

1. INTRODUCTION

The Axial Field Spectrometer (AFS) was recently brought into operation at the CERN ISR. It is being exploited in a wide-ranging programme to study different aspects of those proton-proton or proton-antiproton collisions which are characterized by a large transverse momentum (p_T). Examples include the measurement of inclusive distributions of identified high-p_T hadrons, and the study of event structures characterized by a large transverse energy (E_T) or the production of one or several high-p_T electrons or photons.

Our experimental approach to this programme emphasizes integration of advanced magnetic spectroscopy with state-of-the-art calorimetry. These techniques are fully exploited to provide maximal information on all particles produced. In addition, information from these detectors is used in new ways for on-line event triggering and filtering; this allows even very rare events to be selected with high efficiency, an essential prerequisite for studies at a high-luminosity hadron collider, such as the ISR.

We aimed at considerable modularity of the detectors. Apart from clear advantages of construction, debugging, running, and servicing of such components, modularity provides us with ease for addition or reconfiguration of our system to emphasize the study of specific final states. At present, for example, a 1 sr Čerenkov detector system allows hadron identification up to $p \simeq 12$ GeV/c; liquid-argon electromagnetic calorimeters and a uranium-scintillator calorimeter ("Hexagon") are used for a study of events containing direct photons.

2. AFS COMPONENTS AND THEIR PERFORMANCE

The 1981 layout of the AFS is shown in Figs. 1 and 2. Figure 2 also shows the recently installed low-β insertion, comprising a total of eight superconducting quadrupoles. These are the first superconducting beam elements to be used in a storage ring; they are now operational with colliding beams, producing a sixfold increase in luminosity.

2.1 The open axial field magnet

The design[1] contrasts with earlier magnetic spectrometers for ISR physics[2]*):

---

*) It conforms however to even earlier investigations as summarized by the 12th century scholar William of Occam: "It is in vain to do with more what can be done with less".

COPPER CALORIMETERS

A.P. C.Counter 1 atm.

PROPORT. CH.

ČERENKOV H.P. 4 atm.

URANIUM CALORIMETERS

CENTRAL HODOSCOPE

Č. AEROGEL

VACUUM CHAMBER

DRIFT CHAMBERS

O.A.F. MAGNET

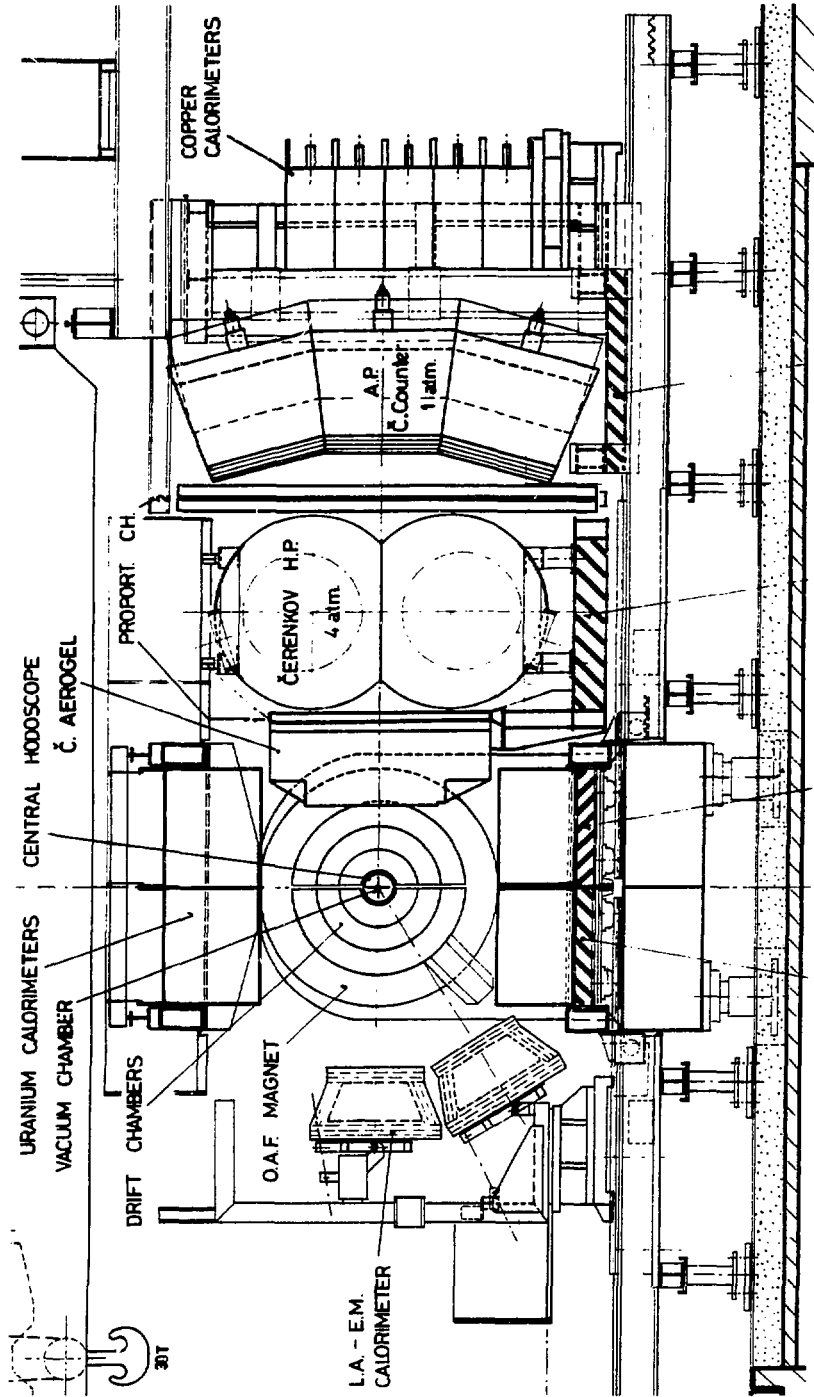L.A. - E.M. CALORIMETER

30T

Fig. 1 Cross-section through the AFS (1981 configuration). The top and bottom U calorimeters (4 ar total) are being installed during the first half of 1981.
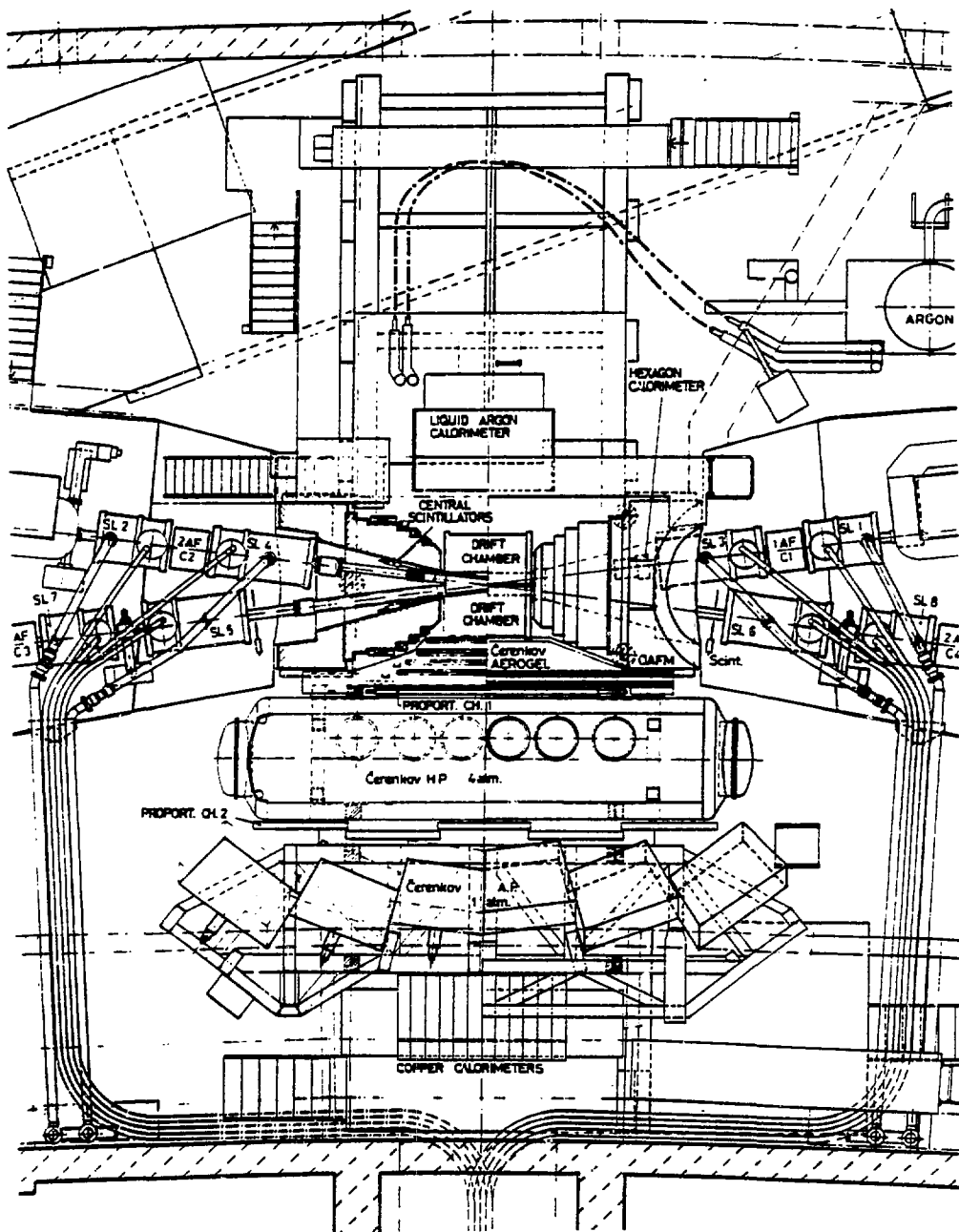
Fig. 2 Top view and horizontal section through the AFS (1981 configuration).
It also shows the position of the eight superconducting quadrupoles (SL1 to
SL8) of the newly operational low-β high-luminosity insertion.

a)   It is a warm magnet because:

-   a magnetic field integral of ≈ 0.5 T·m provides a momentum resolution of
    $\Delta p/p \approx 0.01$ p, which is satisfactory for our physics programme;

-   the low field level facilitates the operation of the drift chamber and
    minimizes effects on the ISR beams, which traverse the field at an angle
    of ±7.5°;

-   it is easier and cheaper to construct and more reliable to operate;

-   it greatly facilitates the implementation of item (b);

b)   Its unique form (Fig. 3) reflects our insistence on integrating the mag-
      netic spectrometer with the surrounding detectors (calorimeters, Čerenkovs)
      by maximizing the totally unobstructed aperture for particle detection,
      even in the forward direction:

$$\text{azimuthal coverage:} \quad 0 \le \phi \le 2\pi$$

$$\text{polar coverage:} \quad 0 \le \theta \le 15° \text{ and } 40° \le \theta \le 140° \ .$$

c)   It allows very rapid access (within 5 min) to the complex central detec-
      tor; this is crucial for the ISR, which is operated continuously, except
      for very short (∿ 2 h) interruptions that are several days apart. It
      allows access to the vacuum pipe in about one hour of time, if machine
      intervention (vacuum, etc.) becomes necessary.

The level and direction of the magnetic field is also shown in Fig. 3.
Over the volume of the vertex detector the field is azimuthally symmetric to
better than 0.5%; the field integral transverse to the particle direction as
a function of polar angle is shown in Fig. 4; approximately constant momentum
resolution is achieved for particles of a *given* p_T for polar angles in the
range 45° < θ < 135°.

The magnet is operated routinely with either polarity, at a single nominal
field level. The field component affecting the circulating beams is corrected
using dipole compensator magnets on either side of the spectrometer; by raising
and lowering the excitation currents simultaneously it is possible to turn the
magnet on and off with stored beams, a feature which is used for checks. The
total power consumption of the magnet system is 700 kW.

2.2 The vertex detector

For completeness we summarize the salient features and refer for more de-
tails to an extended discussion given elsewhere[3]. The physics programme and
the high-interaction rate environment dictated the design considerations. In
particular, the detector was optimized for efficient registration and analysis
of final states with high multiplicity and high particle density ("jets")[4].
This is accomplished by highly redundant non-projective track-point measure-
ments. The azimuthal coordinate perpendicular to the magnetic field is
measured using drift techniques, whereas the coordinate along the drift wire
is obtained with the charge-division method[5]. The 140 cm long cylindrical
chamber (inner active radius 21 cm, outer active radius 80 cm) is organized
in 4° sectors, with 100 μm Cu-Be wires serving as the sector-separating ca-
thodes. Along the radius of such a sector a total of 42 drift wires (30 μm
diameter) measure the track position.

The performance, obtained in high luminosity ISR running (interaction
rate ≳ 800 kHz), is at present found to be:
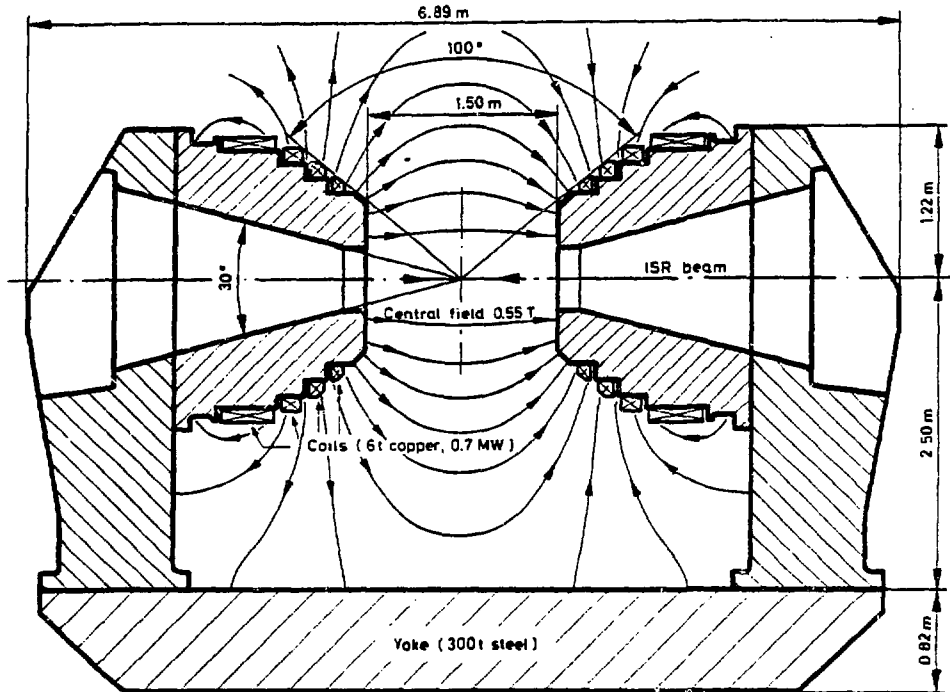
Fig. 3 Vertical cross-section through the open axial field magnet. The magnetic field lines show the direction and level of the field useful for momentum analysis and also the level of "stray field" in the external detectors.
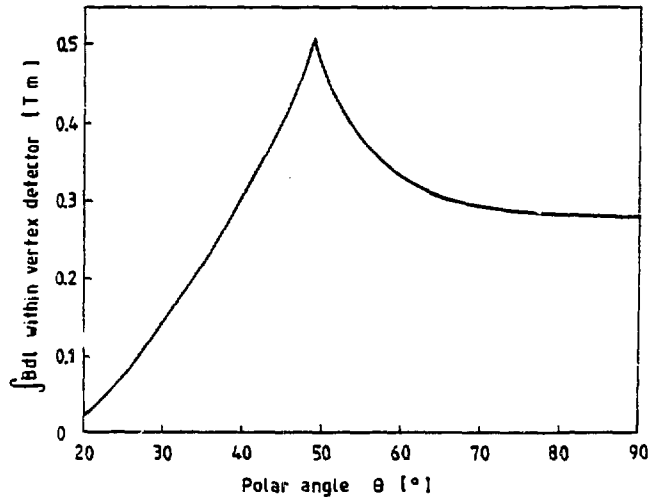

Fig. 4 The magnetic field component transverse to the trajectory of a particle from the vertex, integrated over the radial dimensions of the vertex detector (59 cm) as a function of polar angle (at a nominal power level of 700 kW).

σ(drift) = 200-250 μm,

σ(charge division) = 1.5 cm (at a gas gain of about 2×10^4),

σ(dE/dx) = 11% (truncated mean on tracks with more than 30 ionization measurements),

$\Delta p_T / p_T \simeq 0.02 \ p_T$ (for tracks with more than 35 drift measurements).

Mechanically, the chamber is executed as two semicylinders. This allows rapid extraction of the chamber from the magnet gap, without the need for breaking the ISR vacuum of $\sim 10^{-12}$ Torr. Each half chamber is mounted on a "transparent" support, which also carries 3444 twisted-pair cables from the chamber preamplifiers and which in turn is riding on one half of the "bottom" uranium calorimeter (see Fig. 5). Drift chambers and calorimeters are supported by a chariot riding on precision rails, which ensures positioning of such an assembly with a reproducibility of ≈ 100 μm.
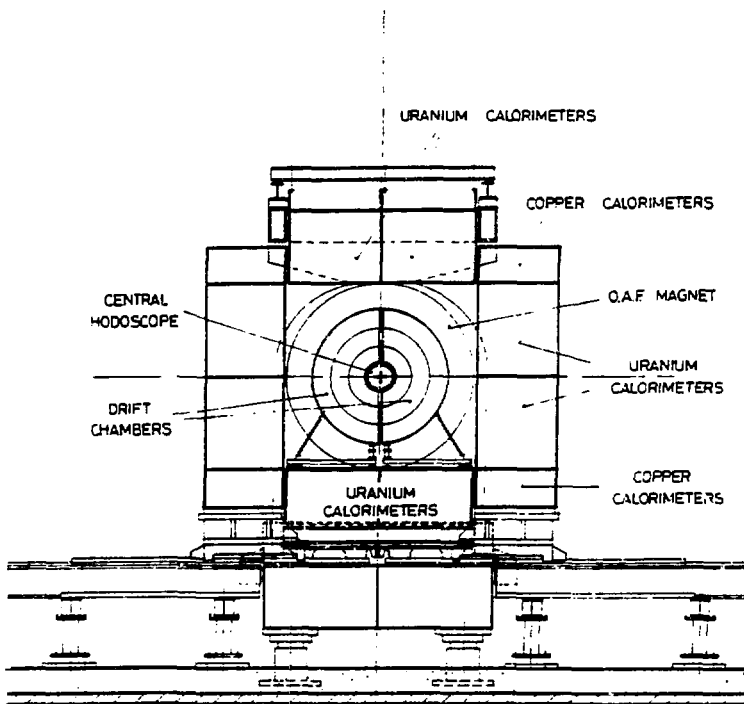

Fig. 5 Cross-section through the AFS showing the drift chamber surrounded by the 2π hadron calorimeter. This layout of the detector is planned for 1982.

2.3 Particle identification

Three threshold Čerenkov counters provide identification of relativistic particles over the solid angle of 1 sr (see Figs. 1 and 2). The first counter contains a radiator of silica aerogel[6]) with a refractive index of n = 1.05; the second is a high pressure counter (HPC) filled with freon-12 at 4 atm with a refractive index of n = 1.004; the third counter is operated, again with freon-12, at atmospheric pressure (n = 1.001, APC). Multiwire proportional chambers (MWPCs) with bidimensional read-out are mounted between the Čerenkov counters and used for triggering and tracking. The counters provide unambiguous identification from 2 to 12 GeV/c.

The relatively high multiplicity of high-p_T events determines the granularity of these counters. The aerogel Čerenkov is subdivided into 20 optical cells, four layers deep, the HPC into 12 and the APC into 18 cells.

Light from the aerogel blocks is projected onto thin wavelength shifters (WLSs); the shifted light is then guided through $\sim$ 2 m long lucite lightguides to low stray field regions, where photomultiplier (PM) operation is relatively easy. Mirror systems are used for both gas Čerenkovs for light collection. Spherical mirrors (typically $\sim$ 2 m^2 surface) focus the light onto flat mirrors, which are viewed by 5 in. PMs at the end of Winston cones. Each cell of the HPC is viewed by two such Winston cone-PM combinations to achieve uniform efficiency for all particles originating from the $\sim$ 60 cm long ISR interaction region. The design goals — uniform and good light collection inside a cell and relative to other cells — have been achieved as verified in extensive beam tests. For the HPC we measure, on an average, 25 photoelectrons for relativistic particles and 15 for the APC. An indication of the performance in the ISR is shown in Fig. 6. A clear separation between pions and heavier hadrons is achieved, although no attempt has been made to remove background from δ electrons and γ conversions.
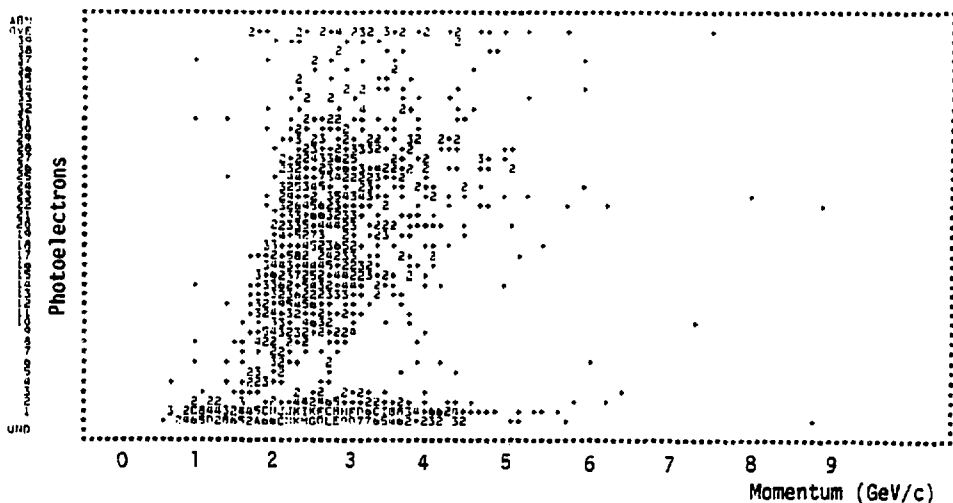

Fig. 6 The ISR performance of HPC, showing the number of photoelectrons as a function of particle momentum. The band of pions is clearly separated from the heavier hadrons.

2.4 The hadron calorimeter

2.4.1 Principal considerations

While there are compelling physics reasons for using hadron calorimeters in colliding beam experiments, lack of adequate instrumental techniques has so far prevented their use. Only in recent years have calorimetry techniques been studied well enough[7], and suitable read-out techniques developed for sampling calorimeters[8]. Effective use of hadron calorimeters at hadron colliders is particularly difficult for the following two reasons:

i) Invariant cross-sections fall steeply as a function of the transverse momentum, typically as p_T^{-9}[9]; measured spectra are smeared by the instrumental resolution and may therefore be grossly distorted (see Fig. 7). Energy resolution is at a premium!
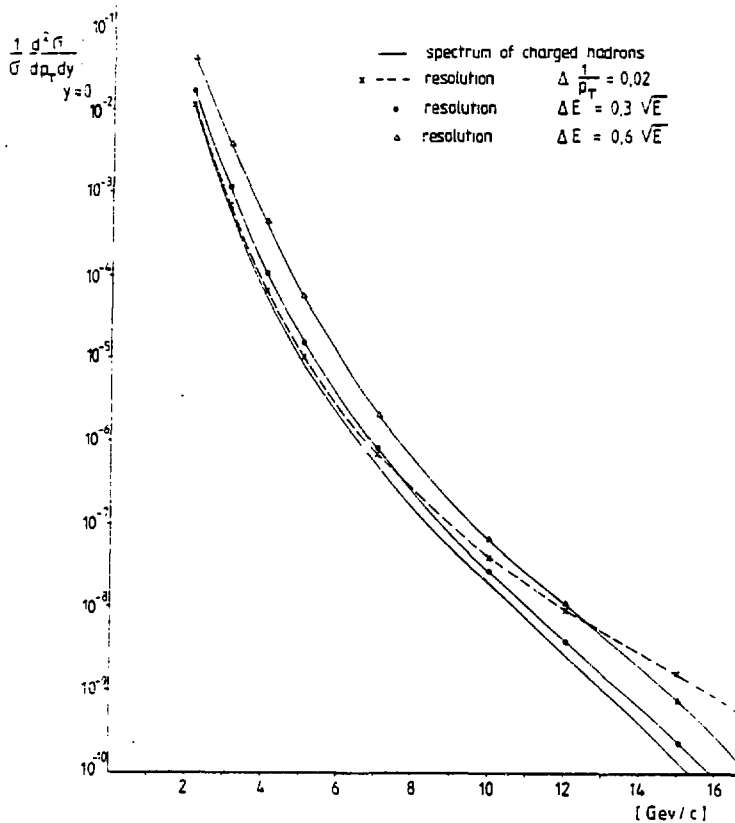

Fig. 7 Effect of detector resolution on a steeply falling particle spectrum, shown for three different resolution functions; $\Delta(1/p) = 0.02$ represents the performance of our drift chamber; $\sigma(E)/E = 0.6/\sqrt{E}$ applies typically for a very good non-U hadron calorimeter, while $\sigma(E)/E = 0.3/\sqrt{E}$ is similar to the resolution of our U calorimeter.

ii) At hadron colliders the calorimeters serve the additional, *equally impor-
    tant role* of very effective and highly selective trigger devices. Again,
    apart from the importance of energy resolution, the unbiased selection of
    final states is only possible if the calorimeter response is independent
    of the nature of the incident particle: a truly democratic response is
    a necessity!

Both of the above requirements are elegantly optimized with the use of ^{238}U as
the absorber plates[7] and we therefore adopted this material.

    Another fundamental consideration is the "granularity" of such a detector,
i.e. the solid angle covered by any read-out channel. The physics suggests a
calorimeter granularity consistent with the measurement of individual particles
even in highly collimated jets. This imposes a relation between the average
absorption length (and hence the transverse dimensions of a hadron shower) and
the average separation between the particles at the entrance face of the
calorimeter. The high average density of our calorimeter ($\bar{\lambda}_{absorpt} = 22$ cm)
and the expected particle density in typical ISR jets of $p_T \approx 10$ GeV/c resulted
in the present design: the entrance face of the calorimeter starts radially
at a distance of 120 cm; the individual cell has an area of 20×20 cm^2 and
resolves $\geq 85\%$ of all particles in a jet.

    2.4.2 Choice of read-out

    Two techniques are available for the active read-out of calorimeters[9]
which do not affect the intrinsic resolution for electromagnetic showers and
which permit a very compact design. The liquid-argon technique, by now matured
into a standard method, has proved its reliability and its excellent control
of systematic effects at the 1% level. Although we considered it as our first
choice, we shied away after initial indications that a surprisingly high
premium would have to be paid for the small U plates required for the ion
chamber electrodes. We settled for second best by adopting the WLS tech-
nique[10,11] for the scintillator read-out.

    The method is sketched in Fig. 8. As with all light-collection techniques,
great care has to be given to:
  i) minimize non-uniformities in the optical elements;
 ii) minimize dead-space introduced by the WLS bar; it must not have excess
     response (produced, for example, by Čerenkov light) to direct particle
     hits;
iii) provide an adequate calibration system for the *complete* read-out chain.

    We arrived at the following optimization[12]. Plastic scintillator*) based
on PMMA (polymethyl methacrylate) was chosen for cost and mechanical reasons.
It was doped with 1% butyl-PBD as the primary scintillating agent and 10%
naphthalene was added to improve the light yield (measured to be about 70% of
NE102A). No wavelength shifting material was used, as is commonly done
("POPOP"), resulting in a desired, strong absorption of the emission spectrum;
we measured for our scintillator an absorption length of $\lambda = 30$ cm, consistent
with our cell size. The WLS was again based on PMMA, doped with BBQ. Suf-
ficiently high absorption of the scintillator light, consistent with adequate
uniformity (±5%) along the WLS and sufficiently low response to Čerenkov light,
was achieved with a 2 mm thick shifter, made from ultraviolet absorbing
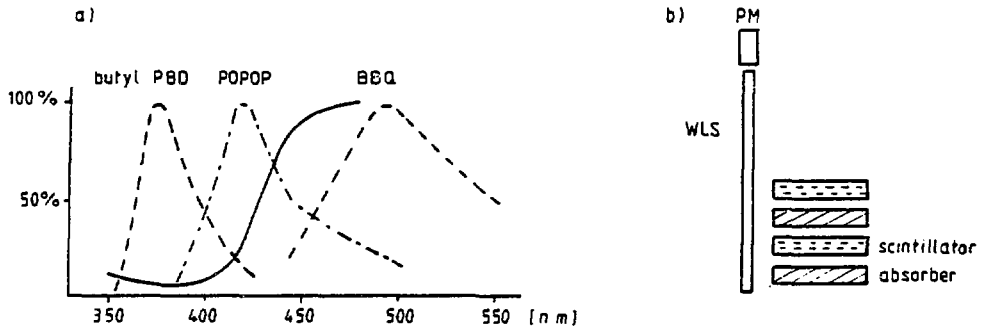
---

*) Manufactured by Altulor S.A., Paris, France.

a)

butyl PBD   POPOP   BBQ

100%

50%

350   400   450   500   550 [n m]

b)   PM

WLS

scintillator
absorber

Fig. 8 Spectral response (a) and conceptual arrangement (b) of the scintillator-
wavelength shifter system for sampling calorimeter. Light emitted from the
scintillator (e.g. butyl PBD or POPOP) enters the wavelength shifter ("BBQ")
across an *air gap*; it is subsequently absorbed and isotropically re-emitted
at longer wavelengths.

plexiglas 201[*]), and doped with 80 mg/ℓ BBQ. Calibration of the *complete*
read-out chain is in general one of the most serious difficulties of this op-
tical technique. We avoided complex auxiliary optical systems by exploiting
the natural radioactivity of our plates as the calibration reference. We find
that in our stacks the charge measured from one of the PMs of the hadronic
part of the calorimeter, during a 10 µs ADC gate, corresponds to the signal
obtained from a ∿ 3 GeV pion. In practice, the U signal of each assembled
stack is cross-calibrated with cosmic-ray muons which establish an absolute
energy scale. From the modules constructed to date, we infer that the U radio-
activity provides an energy calibration at the 1% level.

2.4.3 Mechanical construction of the calorimeter

The solid angle of 8 sr is covered with 128 identical "stacks" (Fig. 9),
arranged in four "walls", as shown in Fig. 5. The corners of the walls are
plugged with smaller stacks made of copper plates to contain approximately 3%
of the energy, which would otherwise escape.

Longitudinally the calorimeter is subdivided into two parts. A 5-radiation-
length deep electromagnetic (e.m.) part is read out separately from the 3.6-
absorption-length deep hadronic section. The final disposition of the plates
in a stack reflects the compromise between the requirements for good energy
resolution and the wish to minimize the total amount of uranium and the re-
quired machining effort. The final optimization resulted in the choice of ten
U plates, 2 mm thick for the e.m. part; the hadronic section consists of 38
cells, each composed of two 3 mm U plates followed by one 5 mm Cu plate.

In the mechanical construction we aimed — not forgetting ease and sim-
plicity — to minimize dead areas due to structural elements inside the stack.
The result is shown in Fig. 10. The plates are tied together with one 10 mm
diameter rod; four 10 mm diameter spacers, located in corresponding holes in
the corners of the scintillator, and one washer, around the central rod, space
the U plates and prevent pressure contact with the scintillators. Constructed
in this way, the stacks are self-supporting in four different positions (Fig. 5).

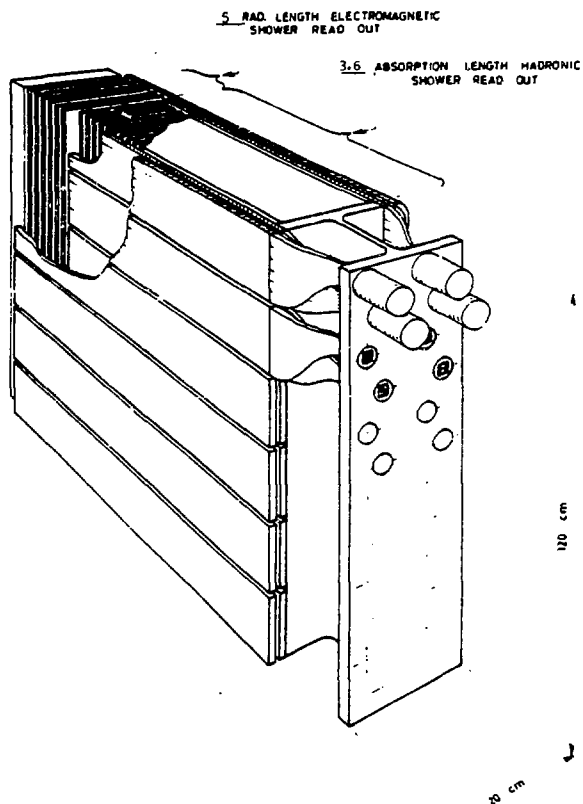*) Manufactured by Röhm GmbH, Darmstadt, Fed. Rep. Germany.

Fig. 9 Sketch of one of 128 calorimeter stacks. Each stack, mechanically homogeneous, is divided optically into 6 cells (20 × 20 cm^2), and each cell is read out on both sides and twice along the longitudinal direction. Note that the electromagnetic part uses ten 2-mm-thick U plates, whereas the hadronic part is composed of seventy-six 3-mm-thick U plates and thirty-eight 5-mm-thick Cu plates. Scintillator of 2.5 mm thickness is used throughout. Each stack weighs about 2 t.

Assembly time, including mounting of the WLSs and PMs, requires eight man-days per stack. So far, we have constructed one wall and completion of the calorimeter is scheduled for the end of 1981.

2.4.4 Performance

Our choice for the light absorption length in the scintillator combined with the read-out arrangement provides excellent *position resolution* in both transverse directions of a stack. An example is shown in Fig. 11, from which one may also judge the optical uniformity of our design. Typically we find for a few GeV/c electrons a spatial resolution of $\sigma_x \approx \sigma_y \approx 10$ mm.
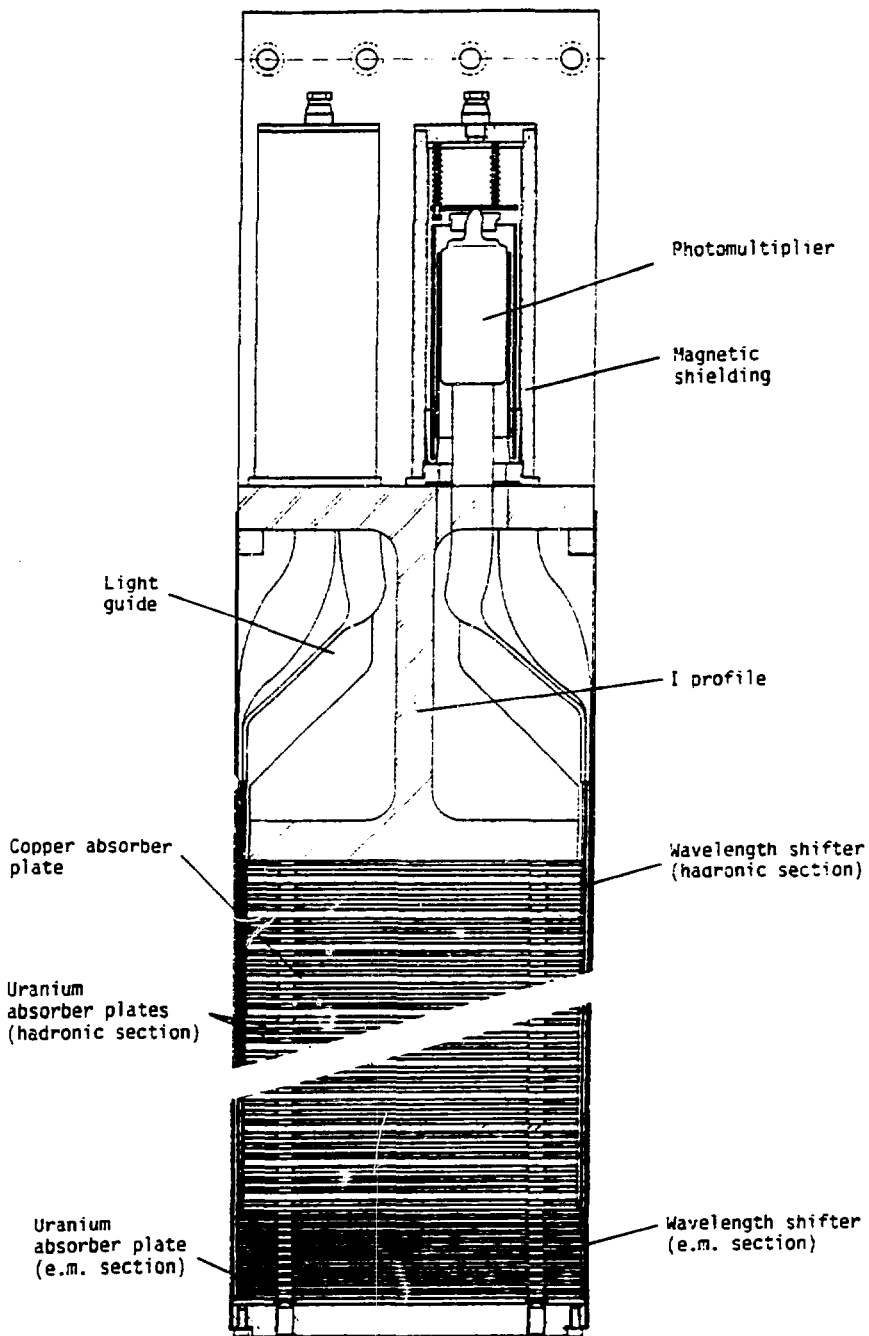
Fig. 10 Horizontal cross-section through a U stack
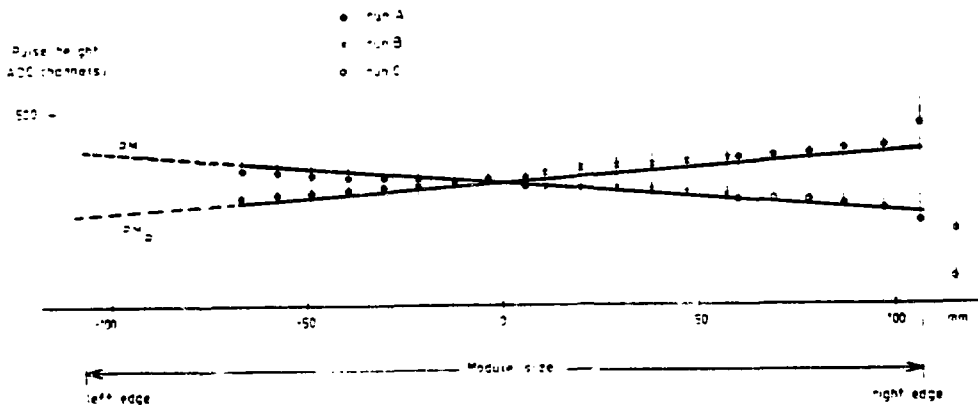
Fig. 11 Mean pulse height as a function of position for 5 GeV/c electrons.
The error bars indicate the FWHM of the pulse-height distributions.
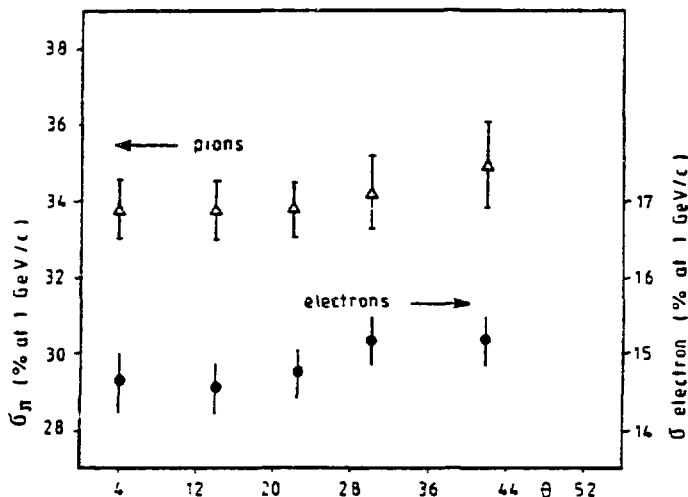
Fig. 12 The normalized energy resolution for electrons and hadrons as a func-
tion of incident angle. The angle θ is measured with respect to normal inci-
dence.

The *energy resolution* for electrons and hadrons as a function of incident
angle into the stack is given in Fig. 12. The electron resolution is consis-
tent with the value expected from sampling and photon statistics (300 photo-
electrons per GeV). The hadronic resolution reflects the intrinsic resolution
of an ideal U calorimeter of

$$\frac{\sigma^U_{intrinsic}}{E} = 0.2/\sqrt{E}_{GeV}$$

and the sampling fluctuations, estimated to be

$$\frac{\sigma^{sampling}}{E} = 0.1 \times \sqrt{\frac{\Delta E \ (MeV) \ gap}{E \ (GeV)}} \approx 0.25/\sqrt{E} \ ,$$

where ΔE is the energy loss per U cell; $\Delta E \approx 6.5$ MeV. The twofold longitudinal read-out combined with good spatial resolution permits considerable electron/pion discrimination. We find a pion rejection of larger than 50 with $\sim$ 80% electron acceptance, if complete shower information is available.

3. THE AFS TRIGGER SYSTEM AND ON-LINE PROCESSORS

The AFS is mostly used to study interactions with cross-sections in the microbarn to nanobarn range, frequently in an environment of very high collision rates (without the low-β insertion a typical luminosity of $L = 2 \times \times 10^{31}$ cm^{-2} s^{-1} implies a particle flux of $> 10^7$ s^{-1} into a 4π detector). Central to efficient study of these relatively "rare" events are trigger and filter schemes, matched in processing power to the primary interaction rate and of sufficient discrimination to permit practical off-line analysis.

On-line processors were developed to evaluate the drift-time information from the central detector, hit patterns from the MWPCs of the Čerenkov arm, and the energy deposition in the calorimeter.

Selection of high-p_T charged particles proceeds through a sequence of increasingly more selective conditions[13]. A rejection of several hundred is obtained in a processing time of less than 1 us, by using position information on the drift and MWPC wires[14]. Ultimate rejection of up to about 5000 is based on the drift-time information for sagitta evaluation with a very fast parallel processor, ESOP[13]. Event purity (i.e. the fraction of tracks with p_T above threshold) is $\sim$ 10%; the trigger efficiency at threshold is $\sim$ 10% and rises to a plateau at $\sim$ 50%. Inclusive spectra up to $p_T = 10$ GeV/c have been recorded in this way.

The trigger processor for the calorimeter is at present being brought into operation. For this purpose the dynode signals from the 3200 individual signal channels are summed over all cells of the same azimuth ("row") for both the e.m. and hadronic segments. This results in 48 primary e.m. signals, and 48 U and 4 Cu-module hadronic signals. These 100 signals are transmitted via air core cable ($v = 0.95c$) to the counting room for further processing. As indicated in Fig. 13, the hadronic sums of adjacent rows are combined, with an overlap of one row. Triggering on energy deposition in such a narrow slice will preferentially select configurations where most of the energy is carried by a single hadron. Similarly, six rows of cells ($\Delta\Omega \approx 1$ sr) are combined into "jet sums" to achieve sensitivity for topologies expected to be characteristic of "jet" structure. Again, a geometrical overlap of 67% in the jet sums minimizes edge effects in the azimuthal efficiency of the trigger. The energy sums provide also a measure of the total deposited energy, E_{tot}, which is used as a pre-trigger and strobe for ADCs. A total of 123 fast, linear sums are generated in this way [48 e.m. single particles (EM), 49 hadronic single particles (SP), 24 jet sums (JET), E_{tot} (E), E_{tot} e.m. (E_{em}), p_T tot (P_T)]. These sums are interrogated by multilevel discriminators (three levels for EM, five SP, four JET, six E, four E_{em}, three P_T), resulting in 493 signals. Subsequently, the definition of the e.m. single particle trigger is refined by requiring a spatial coincidence of an EM signal with a consistent value of an SP. All the information thus obtained is "multiplicity"-encoded, and transmitted in encoded form onto 33 signal lines. Other detectors (MWPCs and drift chambers), and in particular ESOP filtered tracks at different thresholds, may also be correlated with the calorimeter signals for which an additional 17 encoded lines are provided. Logic decisions on the information pattern present
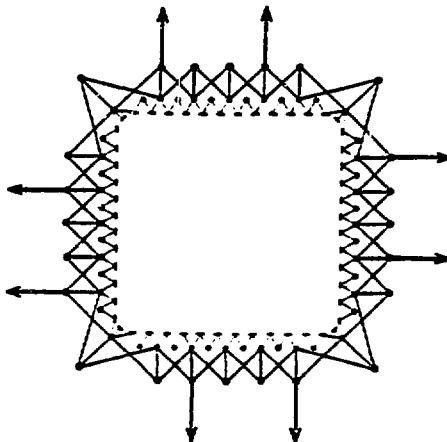
Fig. 13 Schematic diagram of the calorimeter trigger, which uses the information on energy distribution in the transverse plane. A small line segment in the inner square represents the summed up hadronic energy in a "row" of hadronic cells. The lines joining two rows give a "single particle sum", whereas the next level of summing over six rows represents the spatial extension of jets; further summing results in signals representing total energy deposition, E_{tot}.

on these 50 signal lines are carried out by an array of high-speed logic units. Each distinct trigger pattern, represented by a unique signal pattern on the 50 lines, is stored in a 50-bit memory. This arrangement allows parallel decision processing and down-scaling of abundant triggers. A partial list of various representative trigger combinations is provided in Table 1.

Table 1
Selection criteria for some special final states

Experiment	Trigger
1. Identified single-particle inclusive distributions and correlations	$BB \cdot ESOP(1) \cdot 2^{-n}$; $E^i \cdot JET^i(1) \cdot ESOP(1)$; $E^i \cdot SP^j(1) \cdot ESOP(1)$
2. Identified pairs ($\bar{p}p$, $\bar{K}K$, ...)	$BB \cdot ESOP(2)$
3. Jet studies and SP in calorimeter	$BB \cdot 2^{-n}$; $E^i_2{}^{-m}$; $E^j \cdot JET^k(1) \cdot 2^{-r}$; $E^k JET^j(2)$
4. Flavour jets	$E^i \cdot EM^i(1) \cdot ESOP(1)$; $E^i \cdot EM^j(2) \cdot ESOP(2)$
5. Multileptons (≥ 2)	$E^i \cdot E^i_{em} \cdot EM^j(2) \cdot ESOP(2)$
6. Inclusive electrons	$E^i \cdot E^i_{em} \cdot EM^j(1) \cdot ESOP(1) \cdot 2^{-n}$
7. Correlations	$E^i \cdot SP^i(2) \cdot 2^{-n}$; $E^i \cdot JET^k(2) \cdot 2^{-m}$

i) BB stands for "beam-beam" and represents an "unbiased" interaction trigger.
ii) The superscripts i, j, ... indicate the minimum discriminator level and the subsequent higher ones.
iii) Numbers in parentheses specify the multiplicity of a trigger condition.
iv) 2^{-n}, 2^{-m}, ... give the down-scaling factors for abundant triggers.

Data from the drift chamber are recorded in 6888 ADC and 3444 drift-wire recorder channels. Pulse-height information from the full calorimeter will be contained in 3200 ADC channels. Data compaction is achieved on-line by a selective read-out of only those drift wires with a hit, and by using a fast processor to select the corresponding two ADC words; the same processor also groups data into blocks associated with a wire and regroups all the information on an event into a format, which is optimized for off-line analysis. A similar data compression is foreseen for the calorimeter information, using the ESOP processor. In this way the total number of data words is reduced to ∿ 4000 for an average event, but still may be more than double for high-multiplicity events.

4. THE AFS OFF-LINE SOFTWARE

For the present AFS experimental configuration the major part of the off-line data analysis consists of assigning drift-chamber digitizings to tracks, and then determining the momentum. (As calorimeter data become available, the analysis of this information will also constitute a significant part of the off-line programs.)

Sorting the digitizings into tracks is a classic problem of pattern recognition. In the transverse (r, ϕ) plane the track trajectory through the chamber is approximately a circle of radius R (cm) ≈ 700p (GeV/c). Hence for all momenta of interest (≳ 0.3 GeV/c) the radius is much larger than the arc length of the trajectory, which is ≳ 59 cm for a particle traversing the full chamber. Thus the trajectory can be approximated by:

$$\phi = \phi_0 + \alpha r$$

i.e. a *straight line* in r, ϕ coordinates, with a slope related to the particle momentum.

The pattern recognition program proceeds by scanning the r/ϕ plane with a rotating "road", and counting the number of digitizings within the road. A genuine track or track segment will give a large digitizing count. The "left-right" ambiguity is then resolved by requiring the digitizings be smoothly continuous rather than staggered by twice the sense wire staggering. Reasonable continuity in the z coordinate, derived from charge division, is also required at this stage. Finally track segments found within different roads are merged to form the full track. This pattern recognition program takes typically 2 s of IBM 168 time for an event of charged multiplicity 10.

The track digitizings are then passed to the momentum determination program. The procedure used is fairly standard. The time coordinate is eliminated from the equation of motion, resulting in expressions for $d^2(r\phi)/dr^2$ and d^2z/dr^2. The trajectory is interpolated between the measurement points as a polynomial, so that the integration can be done exactly -- the "spline" method. The program then determines the main vertex and secondary (decay) vertices from the fitted tracks. The pulse-height information at the ends of each sense wire, which provides the z coordinate, is also a measure of the energy loss, dE/dx. Given the number of dE/dx measurements, particle identification in the "$1/\beta^2$" region is readily achieved.

It should be stressed that to obtain the best resolution from the chamber, careful studies must be made of topics like:

 i) variation of the drift velocity over the drift region;

ii) pulse-height dependent shifting of the measured time ("slewing");

iii) cross-talk, etc.

The final program in the present chain studies the tracks going into the Čerenkov arm (see Fig. 1). This involves extrapolating the tracks through the various Čerenkov counters and proportional chambers, and identifying the particle. The Čerenkov counters give $\pi/K/p$ separation over the 2-12 GeV/c range.

This large and complex off-line program chain is maintained on four different types of machine (IBM, NORD, UNIVAC, CDC) using the PATCHY system[15].

5. STATUS AND PROSPECTS

During 1981 emphasis is being placed on the measurement of inclusive distributions of high-p_T particles and continuation of studies on events containing direct photons or high-p_T hadrons. The year at the ISR will be marked by the advent of proton-antiproton collisions, with exciting prospects for a number of very topical comparative studies. Physics with the calorimeter will finally begin this year, and subsequent years will see full exploitation of the unique experimental possibilities provided by the 2π calorimeter.

Is something missing from this splendid array of instruments? While clearly a substantial list of interesting detectors could be imagined, one notes in particular the lack of detection facilities for rapidities $|y| > 1.3$. It has been suggested[16] to equip the magnet poles with a fine array of proportional wires, thus extending the calorimeter coverage over two more units of rapidity. Preliminary engineering feasibility studies and test results[17] are encouraging. Recent physics results also remind us of the spatial coarseness of the e.m. part of the calorimeter: direct photons have been discovered at the ISR, and there is even an indication for direct γ-pair production, yet we cannot detect such events with the U calorimeter; J/ψ's and perhaps Υ's are produced predominantly via the excited $q\bar{q}$ states and subsequent de-excitation via γ emission. Although 10^9 $c\bar{c}$ systems and perhaps 10^6 $b\bar{b}$ systems are being produced daily at the ISR, we are blind to such transitions. Soft and hard electrons of varied origins abound, but we have yet to paint a coherent picture and relate it to the underlying constituent dynamics. The list could be prolonged, but all these phenomena could be studied if our present calorimeter were to receive a more fine-grained layer of e.m. shower detection. We are pursuing a variety of options to ensure the uniqueness of the instruments and hence its physics potential even beyond the time when we have stopped observing proton-proton collisions in the CERN ISR.

We are most grateful to the CERN management, who have supported the AFS project with foresight and conviction since its inception.

Our staff at the CERN EP, EF, DD, and ISR Divisions and at the collaborating institutions have worked with competence, dedication, and enthusiasm to provide us with a unique tool for studying high-energy collisions and we thank them for their contributions to the success of the apparatus.

REFERENCES

1) T. Taylor, Contribution to the Workshop on Future ISR Physics, CERN 1976, unpublished note.

2) L. Camilleri et al., Nucl. Instrum. Methods 156, 275 (1978).
    A. Zichichi (Chairman), Results of the ISR working party on a new magnetic facility, CERN 1976, unpublished.

3) H. Gordon et al. (presented by H.J. Hilke), The AFS vertex detector, these proceedings.

4) The chosen geometry is similar to the "jet-chamber" of the JADE Collaboration. See, for example, H. Heintze, these proceedings. We have benefited from discussions with Prof. H. Heintze and his group during the conceptual stages of this detector development.

5) J.C. Berset et al., Nucl. Instrum. Methods 176, 251 (1980).

6) T. Åkesson et al., Performance of the aerogel counter for the CERN AFS, to be published in Proc. Int. Conf. on Experimentation at LEP, Uppsala, 1980.

7) C.W. Fabjan et al., Nucl. Instrum. Methods 141, 61 (1977).

8) For an extensive review, see: S. Iwata, Nagoya Univ. Report DPNU-3-79 (1979).

9) For a comparison, see: C.W. Fabjan and M.G. Fischer, Particle detectors, Rep. Prog. Phys. 43, 1003 (1980).

10) R.C. Garwin, Rev. Sci. Instrum. 31, 1010 (1960).

11) First test results of this read-out technique were reported by: A. Erwin et al., Proc. Calorimeter Workshop, FNAL, 1975 (FNAL, Batavia, Ill., 1975).

12) O. Botner et al., Nucl. Instrum. Methods 179, 45 (1981).

13) B. Heck et al., Invited contribution to be published in Proc. Europhysics Conf. on Computing in High Energy and Nuclear Physics, Bologna, Italy, 1980.

14) S. Jaroslawski, Nucl. Instrum. Methods 176, 263 (1980).

15) H. Klein and J. Zoll, PATCHY Manual, CERN Program Library, January 1977.

16) I. Polk and W. Willis, ISABELLE Technical Note, unpublished.

17) T. Ludlam et al., BNL-28605, and to be published in Proc. IEEE Nucl. Science Symposium, Orlando, Florida, 1980.